Precision measurement of charge symmetry breaking in *np* elastic scattering at 347 MeV

J. Zhao,[1,*] R. Abegg,[2,†] A. R. Berdoz,[1,‡] J. Birchall,[1] J. R. Campbell,[1] C. A. Davis,[1,2] P. P. J. Delheij,[2] L. Gan,[1] P. W. Green,[3] L. G. Greeniaus,[3] D. C. Healey,[2] R. Helmer,[2] N. Kolb,[3,§] E. Korkmaz,[3,‖] L. Lee,[1] C. D. P. Levy,[2] J. Li,[3,¶] C. A. Miller,[2] A. K. Opper,[3,**] S. A. Page,[1] H. Postma,[4] W. D. Ramsay,[1] J. Soukup,[3] G. M. Stinson,[3] W. T. H. van Oers,[1] and A. N. Zelenski[2]

[1]*Department of Physics, University of Manitoba, Winnipeg, Manitoba, Canada R3T 2N2*

[2]*TRIUMF, 4004 Wesbrook Mall, Vancouver, British Columbia, Canada V6T 2A3*

[3]*Department of Physics, University of Alberta, Edmonton, Alberta, Canada T6G 2N5*

[4]*Laboratory for Technical Physics, Technical University Delft, 2600 GA Delft, The Netherlands*

(Received 31 January 1997; revised manuscript received 22 October 1997)

A nonzero difference of the analyzing powers due to charge symmetry breaking has been measured with high precision in *np* elastic scattering at a neutron beam energy of 347 MeV. The neutron beam and proton target were alternately polarized for the measurements of A_n and A_p. A mirror-symmetric detection system was used to cancel geometry-related systematic errors. From fits of the measured asymmetry angular distributions over the range of $53.4° \leqslant \theta_{cm} \leqslant 86.9°$, the difference in the zero-crossing angles of the analyzing powers was determined to be $0.438° \pm 0.054°(\text{stat.}) \pm 0.051°(\text{syst.})$ in the center-of-mass system. Using the experimentally determined slope of the analyzing power $dA/d\theta = (-1.35 \pm 0.05) \times 10^{-2}$ deg^{-1} (c.m.), this is equivalent to $\Delta A \equiv A_n - A_p = [59 \pm 7(\text{stat.}) \pm 7(\text{syst.}) \pm 2(\text{syst.})] \times 10^{-4}$. The shape of $\Delta A(\theta)$ in the vicinity of the zero-crossing angle has also been extracted. Predictions of nucleon-nucleon interaction models based on meson exchange agree well with the results. [S0556-2813(98)06404-8]

PACS number(s): 13.75.Cs, 11.30.Hv, 13.88.+e, 21.45.+v

I. INTRODUCTION

In quantum chromodynamics (QCD), the underlying theory of the strong interaction, each and every violation of isospin symmetry has as its origin the mass difference of the up and down quarks and the electromagnetic interactions among the quarks. In QCD the charge symmetry operation corresponds to the exchange of up and down quarks

$$P_{CS}|u\rangle = -|d\rangle, \quad P_{CS}|d\rangle = |u\rangle. \tag{1}$$

The study of isospin symmetry has been pursued both experimentally and theoretically for a long time. Much evidence has been accumulated over the years that charge symmetry in general holds to the order of 1% (see various recent review papers [1–4]). Detailed tests should establish not only the degree to which isospin symmetry is broken, but also should establish the behavior of the isospin symmetry breaking amplitude as a function of the kinematical variables.

The present paper reports on a precision measurement of charge symmetry breaking (CSB) in *np* elastic scattering at 347 MeV (For a first account see Ref. [5]). The *np* system is a two-body system without the Coulomb interaction. Charge symmetry breaking in the *np* system belongs to a different class of isospin symmetry breaking than in the comparison of the *nn* and *pp* systems. In the *np* system, charge symmetry leads to the equality of the analyzing powers for polarized neutrons scattering from unpolarized protons and vice versa. Any difference in the analyzing powers,

$$\Delta A \equiv A_n - A_p, \tag{2}$$

will signify the breaking of charge symmetry. The magnitude of ΔA is expected to be small, generally less than a percent. Therefore, control of systematic errors is critical. Designed as a null experiment, the difference of the analyzing powers was determined at the zero-crossing angle, the angle at which the average of the analyzing powers vanishes, $\langle A \rangle = 0$. In general to measure ΔA to the accuracy of 10^{-4}, the polarization needs to be known to a similar level, which is unattainable at present. The difference of the asymmetries and the difference of the analyzing powers has the following simple relation:

$$\Delta \epsilon = \frac{1}{2}\langle P_{\text{beam}} + P_{\text{target}} \rangle \cdot \Delta A(\theta) + (P_{\text{beam}} - P_{\text{target}}) \cdot \langle A(\theta) \rangle. \tag{3}$$

However, at the zero-crossing angle, the second term and associated systematic errors disappear. Rather than measuring ΔA directly at the zero-crossing angle, the difference of the individual zero-crossing angles, where the respective analyzing powers cross zero,

*Present address: Laboratory of Nuclear Science, Massachusetts Institute of Technology, Cambridge, MA 02139.

†Deceased.

‡Present address: Department of Physics, Carnegie-Mellon University, Pittsburgh, PA 15213.

§Present address: Department of Physics, University of Saskatchewan, Saskatoon, S7N 0W0, Canada.

‖Present address: Department of Physics, University of Northern British Columbia, Prince George, B.C., V2N 4Z9, Canada.

¶Present address: R.R. Donnelley & Sons Company, Chicago, IL 60601.

**Present address: Department of Physics, Ohio University, Athens, OH 45701.

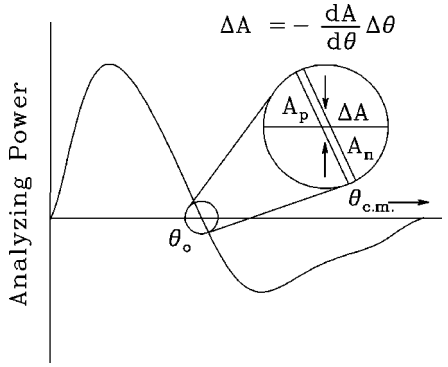

FIG. 1. An illustration of the method employed to extract $\Delta A \equiv A_n - A_p$ from the difference, $\Delta\theta_{\circ}$, in the A_n and A_p zero-crossing angles for np elastic scattering. $dA/d\theta$ is taken from phase-shift analyses or determined experimentally; $\Delta\theta_{\circ}$ is measured in the experiment.

$$\Delta\theta_{\circ} \equiv \theta(A_n = 0) - \theta(A_p = 0), \tag{4}$$

is measured. The two measurements, with either the neutron beam polarized or the proton target polarized, were interleaved and performed with the same detector system and identical beam and target properties (except polarization). The difference of the zero-crossing angles, $\Delta\theta_{\circ}$, is related to the difference ΔA by

$$\Delta A = -(dA/d\theta)\cdot\Delta\theta_{\circ}. \tag{5}$$

Figure 1 illustrates the method of deducing ΔA from the measured difference of the zero-crossing angles of the analyzing powers.

The first measurement of charge symmetry breaking in np elastic scattering, was carried out at TRIUMF at 477 MeV [6]. That experiment yielded $\Delta A = [47 \pm 22 \pm 8] \times 10^{-4}$ from data in the angular range of $59° - 80°$ in the center-of-mass system. The result is a little over two standard deviations from zero. It demonstrated CSB caused by nonelectromagnetic terms of the class IV force in the classification scheme of Henley and Miller [2] (see below). A similar experiment was carried out at the Indiana University Cyclotron Facility (IUCF) in np elastic scattering at 183 MeV [7]. Data were taken with beam and target polarized simultaneously, and spin observables were extracted. The result reported, $\Delta A \equiv A_n - A_p = [34.8 \pm 6.2 \pm 4.1] \times 10^{-4}$ [8] is an average over an angular range in the center-of-mass system from 82.2° to 116.1°, for which the average of the analyzing powers, $\langle A \rangle$, is equal to zero. This represents a CSB effect of 4.5 standard deviations and differs from the contribution expected from the electromagnetic spin-orbit interaction alone by 3.4 standard deviations. It represented the strongest experimental evidence of charge symmetry breaking in np elastic scattering and the most clear-cut observation of class IV CSB interactions. At 183 MeV, a $\rho^{\circ} - \omega$ mixing contribution to ΔA was clearly observed (an approximately two standard deviation effect). The shape of ΔA was also extracted in the IUCF experiment.

NN potentials have been classified by Henley and Miller [2] into four classes according to their transformation properties under isospin symmetry operations. The potential which is responsible for CSB in the np system is the so-called class IV potential which can be written in the form

$$V_{\mathrm{IV}} = e[I_3(i) - I_3(j)] + f[\vec{I}(i) \times \vec{I}(j)]_3. \tag{6}$$

This potential breaks both charge symmetry and charge independence and causes mixing of isospin. In a two-body system, the potential causes the mixing of ${}^1L_j$ and ${}^3L_j$ states (e.g., ${}^1P_1$-${}^3P_1$, ${}^1D_2$-${}^3D_2$, ${}^1F_3$-${}^3F_3 \cdots$). The potential will only affect the np system and has no effect on the nn or pp systems. After taking consideration of the time reversal invariance of the class IV potential expressed above, the potential can be written in the form

$$V_{\mathrm{IV}} = [I_3(1) - I_3(2)][\vec{\sigma}(1) - \vec{\sigma}(2)]\cdot\vec{L}v(r) + [\vec{I}(1) \times \vec{I}(2)]_3[\vec{\sigma}(1) \times \vec{\sigma}(2)]\cdot\vec{L}w(r). \tag{7}$$

Here σ denote the Pauli spin matrices for nucleons, $\vec{L}$ is the angular momentum, and $v(r)$ and $w(r)$ are scalar operators independent of spin and isospin.

In recent years, various attempts have been made to use quark degrees of freedom to evaluate CSB effects [9]. These calculations are still qualitative and very model dependent. At low and intermediate energies, meson exchange *NN* potential models have been applied and more reliable predictions can be provided [10–15]. Calculations show that the most important contributions are due to: (a) one-photon exchange, the electromagnetic interaction between the proton charge current and the neutron magnetic moment, (b) one-pion exchange, the np mass difference in charged one π exchange, this term has major contributions to ΔA at the energies of the TRIUMF experiments; and (c) meson mixing, arising from the isospin mixing of the neutral vector mesons ρ° and ω. It is believed that the up-down quark mass difference has crucial contributions to $\rho^{\circ} - \omega$ mixing [3,9]. This term gives an angular distribution similar to the shape of the analyzing power $A(\theta)$ for energies above 300 MeV. It therefore changes sign near the zero-crossing angles of $\langle A(\theta) \rangle$. However, at 183 MeV, the IUCF experimental energy, the $\rho^{\circ} - \omega$ mixing angular distribution changes sign at a center-of-mass angle of 75° whereas $\langle A(\theta) \rangle$ changes sign near 97°; it accounts for about 40% of ΔA at the zero-crossing angle. $\pi - \eta$ mixing generates a class III potential and therefore does not contribute to ΔA [10], assuming one-boson exchange. The np mass difference affecting charged ρ exchange gives rise to a class IV potential, but its effect is much smaller than in one-pion-exchange. Other processes including 2π exchange and indirect quark effects have been calculated and shown to be small. Contributions due to $\gamma - \pi$ exchange have been calculated and are shown to contribute only in second-order processes [16].

The one-boson-exchange model has provided quantitatively satisfactory predictions of CSB in the *NN* interaction. In particular, the short range $\rho^{\circ} - \omega$ mixing has to be included in the calculation to interpret the IUCF experimental result. Using complex phase-shift amplitudes, it has been shown that inelasticity changes the value of ΔA by at most 10% at 800 MeV; its effects become vanishingly small at lower energies (i.e., 477 MeV or below) [17].

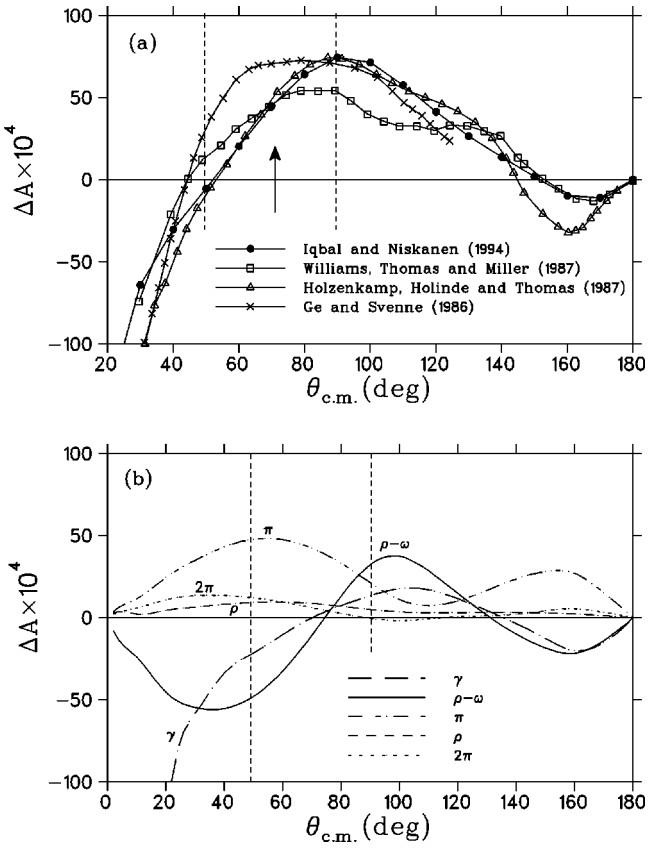

FIG. 2. (a) A comparison of various predictions for ΔA at 347 MeV; the dashed lines show the angular range covered in this experiment and the arrow shows the position of the zero-crossing angle; (b) different contributions to ΔA as predicted by Iqbal and Niskanen [15].

In Fig. 2(a), various predictions of ΔA at 347 MeV based on meson exchange NN potential models, by Williams, Thomas, and Miller (WTM [12,11]), Holzenkamp, Holinde, and Thomas (HHT [13]), Ge and Svenne (GS [14]), and Iqbal and Niskanen (IN [15]), are compared. Figure 2(b) shows the different contributions to ΔA at 347 MeV as calculated by Iqbal and Niskanen [15]. The treatment of the electromagnetic term accounts for much of the WTM-GS difference. The WTM-HHT difference is due to the treatment of the ρ and $\rho^\circ-\omega$ terms.

Concerns [18] have been raised regarding the application of the on-shell meson mixing amplitudes to off-shell virtual process such as $\rho^\circ-\omega$ mixing. The exchanged vector meson has a spacelike momentum, far from the on-shell point. In all prior calculations, it was customary to assume that the $\rho^\circ-\omega$ mixing amplitude is a constant over the whole range of four-momentum transfers. The on-mass-shell vector meson $\rho^\circ-\omega$ mixing was extracted from the cross-section measurement of the reaction $e^+e^-\rightarrow\pi^+\pi^-$ [19]. The strong interaction contribution to the mixing amplitude is then $\langle\rho^\circ|H_{\rm str}|\omega\rangle=-(5160\pm620)$ MeV^2 [4]. Recent calculations [20–26] reveal a node at or near $q^2=0$, with a consequent change in the sign of the mixing amplitude. This off-shell effect will cause the $\rho^\circ-\omega$ mixing contribution to CSB to vanish or to become significantly smaller than the value that is obtained using the on-shell mixing amplitude. On the other hand, it has been argued [4,27] that current experimental results support the previous calculations with on-shell mixing amplitudes and that various calculations of off-shell effects have imperfections and need support from experimental results. For instance, Coon and Scadron [28] argue that more exact calculations will give results that do not differ much from those which use the on-shell mixing amplitude. More recently, it has been shown [29] that other effects (e.g., isospin-violating meson coupling constants) would also contribute to ΔA. This might offset the deficit in the contribution to ΔA due to off-shell effects. It has also been argued that mesonic width effects will influence the momentum dependence of the $\rho^\circ-\omega$ mixing matrix elements [30].

II. EXPERIMENTAL ARRANGEMENT AND PROCEDURE

The experiment was performed with a 347 MeV neutron beam scattering off a frozen spin proton target (FST). The neutron beam and the proton target were alternately polarized for the measurements of A_n and A_p. Identical beam properties and target composition (except for polarizations) and the same detection system were used for these interleaved measurements. Scattered neutrons and recoil protons were detected in coincidence using a mirror-symmetric detection system to cancel geometric systematic errors. Frequent flip of the neutron beam or proton target spin directions further canceled systematic errors not correlated with the spin direction. At the zero-crossing angle, all systematic errors, except those due to background corrections and effective beam energy considerations (see Secs. III C and III D), were eliminated to second order in an expansion in the error contributions. The protons were detected by a time-of-flight (TOF)/range telescope and the neutrons were detected by a scintillation detector array. Figure 3 shows schematically the beam line and the detection system. The following subsections will describe in detail the beam production and beam transport system, the beam monitors, and the data-taking detectors (see also Ref. [31]).

A. Proton beam production and transport system

Polarized H^- ions were obtained from the TRIUMF optically pumped polarized ion source (OPPIS) [32]. A beam intensity of 40 μA with a normalized emittance of about 0.8 π mm mrad) at the source (an intensity of 15 μA at the injection with an acceptance of about 0.3 $\pi\cdot$mm mrad), and polarization as high as 80% were achieved. The polarization was measured by a low-energy polarimeter based on the ^{6}Li$(p,^3$He$)\alpha$ reaction [33]. To minimize the possible correlation of beam position changes with spin direction reversals, proton spin direction reversals were achieved at the ion source by changing the wavelength and helicity of the optical pumping laser light. A typical spin polarization cycle consisted of polarized:unpolarized:polarized beam periods of durations 60:15:60 seconds. Every polarization ''on'' state (spin up or down chosen randomly at OPPIS) was followed by a polarization ''off'' state (unpolarized beam).

During acceleration, there is a loss in polarization (about a few percent) due to several cyclotron depolarizing resonances. In the present experiment, a phase-restricted tune was used [34] to keep the beam bunch time width within 1 ns full width at half maximum (FWHM) (beam bunch separa-

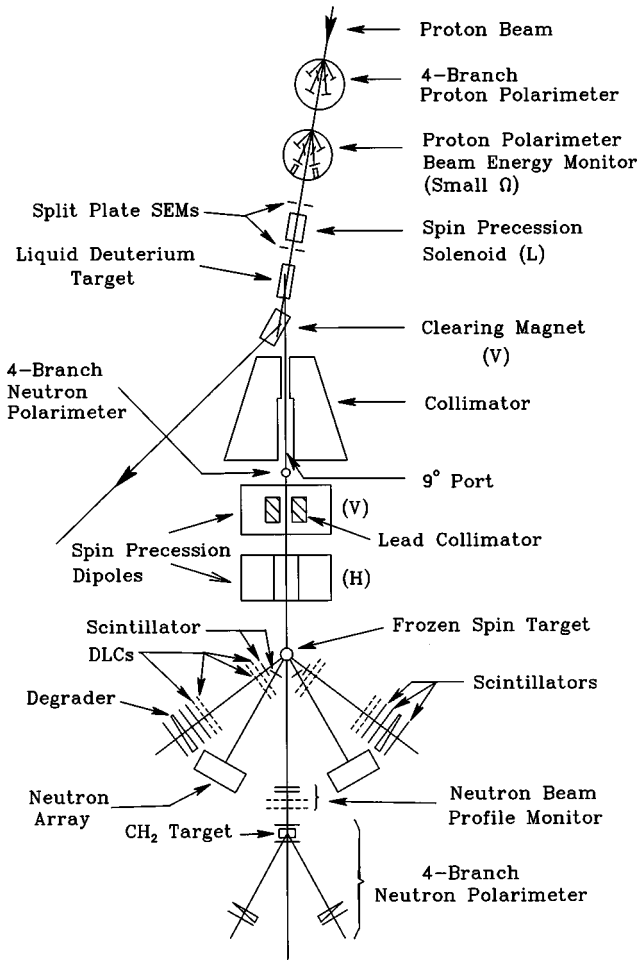

FIG. 3. Layout of the beam transport system and schematic view of the experimental apparatus.

tion of 43 ns). At the neutron production liquid-deuterium (LD_2) target, the 369 MeV proton beam had a polarization of about 75% with currents up to 2.5 μA.

B. Neutron beam production and collimation

A polarized neutron beam with an average energy of 347 MeV and FWHM of about 11 MeV was produced using the reaction $D(\vec{p},\vec{n})2p$. The density of the target was kept stable (to ± 0.0005 g/cm^3) since density changes would affect the average neutron beam energy and therefore the zero-crossing angles. A neutron beam intensity of about $10^5/(\mu\text{A}\cdot\text{cm}^2\cdot\text{s})$ at the FST was achieved. To take advantage of the large sideways to sideways spin transfer coefficient (r_t) of the $D(\vec{p},\vec{n})2p$ reaction, (for the 364 MeV proton energy at the center of the LD_2 target, r_t at 9° lab. is $-0.880 \pm 0.010(\text{stat.}) \pm 0.011(\text{syst.})$ [35]), the proton spin polarization was rotated from the normal direction (vertical transverse direction) into the scattering plane (horizontal transverse direction) by a superconducting solenoid.

The neutron beam was defined by a collimator at 9° with respect to the proton beam. The apertures used in the experiment ranged in size from 39.1 mm (horizontal)$\times$22.5 mm (vertical) to 46.1 mm$\times$37.3 mm, to approximate a tapered shape over the collimator length of 3.35 m. The neutron beam profile, neutron beam energy, and polarization were monitored continuously during data taking and also checked against Monte Carlo simulations [36].

C. Proton polarimeter and beam energy monitor

In principle, the value of the beam polarization was not required for the measurement of the zero-crossing angle difference, but in fact it was measured as accurately as possible to control systematic errors. The two polarimeters used in the experiment were labeled IBP and CSB [37,38]. The CSB polarimeter was a two-branch system which included a beam energy monitor (BEM) and was used to monitor the proton beam transverse vertical polarization and the beam energy.

Because of the carbon content in the polarimeter target material, an effective analyzing power was required to account for the contribution of $C(p,2p)$ quasielastic scattering to the measured asymmetry. To calibrate the polarimeter, different targets with differing hydrogen to carbon ratios were used, i.e., polyethylene (CH_2), kapton ($C_{22}H_{10}N_2O_5$), and pyrolitic-graphite (C) targets. Calibrations were made several times during each data taking period. Instrumental asymmetries of the polarimeters were determined using the unpolarized state of the incident proton beam.

The IBP was a four-branch polarimeter and measured both left-right and down-up asymmetries. Its design principle was similar to that for the CSB polarimeter, but it had larger solid angle coverage. The accidental coincidence rates were kept to an acceptable level by using thin para-xylylene-N [39] targets [$(CH)_x$, ~ 200 μg/cm^2]. The IBP gave results consistent with the CSB polarimeter.

Since the zero-crossing angles of the analyzing powers change significantly with beam energy ($d\theta_\bigcirc/dE_{n\text{beam}} \simeq 0.048°$/MeV [40]), the proton beam energy was monitored by the beam energy monitor (BEM) [38] and kept stable within ± 0.05 MeV by small adjustments of the cyclotron rf or slight changes of the stripping foil position. The proton beam energy was 368.3 ± 1.0 MeV as obtained from a calibration of the cyclotron beam-extraction stripping-foil position [41,42].

D. Proton beam position and secondary emission monitors

A shift in the beam position and/or direction, especially when correlated with the reversal of the proton beam spin direction could cause significant systematic errors. Therefore, two split plate secondary electron emission monitors (SEM's) [43,44] and a feedback system were installed in the proton beam line to monitor and stabilize the proton beam position and direction at the LD_2 target. The proton beam position at the LD_2 target was stabilized to within 0.05 mm by the two SEM's and the fast feedback system controlling two horizontal and two vertical steering elements.

E. Phase lock system

Timing with respect to the cyclotron rf system was needed to monitor the proton beam pulse width and to calculate the incident neutron beam energy. A specially designed electronic module shifted the phase of the rf signal such that a constant time difference was maintained between

a scintillation counter (installed in the 6° port of the neutron collimator) signal and the rf signal.

F. Neutron polarimeter and profile monitor

The neutron beam polarization and profiles were monitored by two neutron polarimeters, labeled NEW and OLD, and a neutron profile monitor [31]. The NEW neutron polarimeter was located at the exit of the collimator, and the OLD was located 4.07 m downstream from the FST (Fig. 3) and thus after the spin precession dipole magnets. The neutron profile monitor was located directly upstream of the OLD neutron polarimeter, 3.65 m downstream of the FST. Both neutron polarimeters were based on the same principle and had a similar design, consisting of four branches in the horizontal and vertical planes to measure left-right and down-up asymmetries of the recoil protons produced by (n,p) reactions in a CH_2 target. The effective analyzing powers of the neutron polarimeters were derived from the measured asymmetries, the measured proton polarization, the known spin-transfer coefficients and the calibrated spin precession magnet settings. A stability and consistency of a few percent for the value of P_n in the neutron polarization measurement was achieved with both polarimeters.

The neutron profile monitor was used to monitor the horizontal and vertical neutron beam intensity distributions and their centroids. All detectors of the profile monitor were aligned to the neutron beam axis.

G. Frozen spin target

The frozen spin target (FST [45]) cell was 35 mm long, 20 mm wide, and 50 mm high and contained 3.5×10^4 mm^3 of 2-mm-diameter butanol beads immersed in a bath of 94% ^{4}He and 6% ^{3}He refrigerant. The butanol beads had a packing fraction of 0.59. The volume occupied by the butanol beads in the target cell was determined from x-ray radiographs taken before, during and after each major data-taking period. The neutron beam fully illuminated the entire inner target canister but not the sides of the outer 80 mm diameter, 120 mm high flask. A holding field of 0.227 T was used during the experiment and a polarization up to 90% and a decay time of >200 h at a temperature of approximately 55 mK were attained. The polarization of the FST was measured by an NMR system after the target was polarized and before it was depolarized. The NMR system was calibrated at a temperature of 1.36 K and a magnetic field of 2.51 T, giving a proton polarization of 0.19%. The procedure of the NMR measurements was cross calibrated in a pp elastic scattering experiment to an accuracy of 2.6% [46].

H. Proton detection system

The recoil protons were detected by two proton time-of-flight (TOF)/range counter telescopes, placed mirror symmetrically with respect to the beam axis. Along the recoil proton tracks, each telescope included a TOF ''start'' scintillator (pTOF), four delay line wire chambers (DLC's) for proton track reconstruction (see Ref. [47] for details), two scintillator E counters as proton TOF ''stop'' counters, a wedge-shaped brass degrader to stop protons from np elastic scattering and a veto scintillator to reject high-energy background off-line. The degrader was made such that its wedge shape compensated the kinematic spread of the energies of the recoil protons from elastic scattering. The proton detection systems were supported by aluminum booms centered at $\pm53.00°$ in the laboratory frame. Figure 4 is a detailed view of the detector system. The pTOF and E counters were placed at radial distances of 0.30 and 1.70 m, respectively, (the actual positions of the proton detectors were measured to better than ±1 mm and $\pm0.02°$), with respect to the pivot which coincided with the intersection of the FST axis and the neutron beam axis. The four DLC's on each arm were placed in two groups. The front DLC's were at radial distances of 0.50 and 0.66 m and the rear DLC's were placed at radial distances of 1.40 and 1.57 m, respectively. The dimensions of various proton detectors is given in Table I.

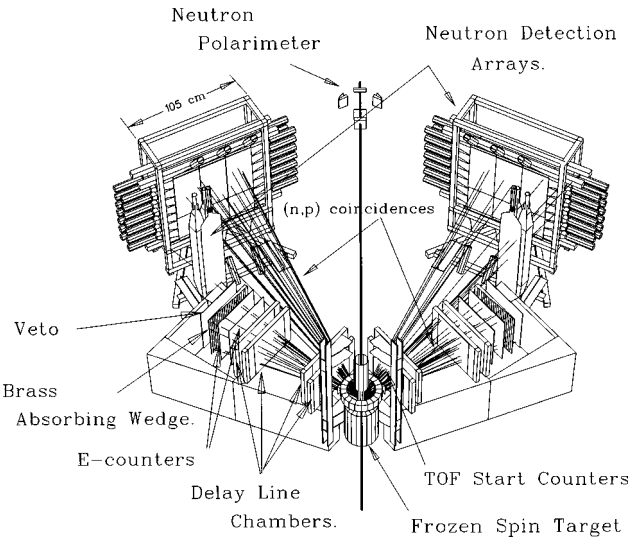

FIG. 4. A detailed view of the detection system.

The pTOF with two photomultiplier tubes (PMT's) (top and bottom) and the two E counters with four PMT's each (two top and two bottom) defined the trigger of the recoil protons and gave the time-of-flight (TOF) for the protons between the pTOF and the E counters. The latter were separated by 1.419 and 1.572 m for the physical right arm and by 1.416 and 1.571 m for the physical left arm, respectively. After the calibration and correction for the position dependence of the scintillation light traveling in the E counters, an average energy resolution of about $\sigma=9.0$ MeV in the recoil proton energy measurements or 0.6 ns in their time-of-flight was achieved.

TABLE I. Dimensions of the proton detectors (in mm).

Detector	Thickness×Width×Height
PTOF	1.6×130×152
DLC's	(a)×580×580
E_I	6×670×650
E_{II}	6×670×690
VETO	6×670×690

[a]Thickness equivalent to 250 mg/cm^2 Al for 50–250 MeV protons [47].

I. Neutron detection system

The scattered neutrons were detected by two large position-sensitive neutron scintillator arrays located left-right symmetrically with respect to the beam axis. Each side consisted of a main neutron array and an auxiliary array centered at $\pm 29.5°$ and $\pm 40.0°$ with respect to the beam axis and located at 3.96 and 3.02 m (centers of the detectors) from the center of the FST, respectively (Fig. 4). The actual positions were measured to better than ± 2 mm and $\pm 0.03°$.

The main neutron detection array [31] consisted of two banks of NE110 scintillator bars, one behind the other, with seven horizontal bars stacked in each bank. Each scintillator bar was 1.05 m long$\times$0.15 m high$\times$0.15 m thick and was optically isolated from the others. The main array was preceded by scintillator panels to veto incident charged particles. Small scintillators (button counters) mounted centrally behind the second bank detected passing charged particles for gain control. Each auxiliary array consisted of two vertical scintillator bars (BC412), one beside the other. Each bar had an identical geometry and light guide as the scintillator bars in the main array. The auxiliary arrays had their own separate veto and button counters.

The detection efficiency of the neutron detector system was estimated with a Monte Carlo simulation code [48]. A single layer of neutron scintillation bars had an efficiency of about 16% and two banks combined had an average efficiency of about 30% with a reasonable threshold of 0.4–1.1 MeV electron equivalent (MeVee). The hardware threshold was about 0.4 MeV and the software thresholds used in data analysis were 0.4–1.1 MeVee.

J. Run procedure

A number of tests and calibrations were made for the DLC's, spin precession magnets, and various detectors and monitors. Final data taking took place in three consecutive periods, each of which spanned about a month of beam time.

Possible systematic errors could arise from spin-correlated changes in the neutron beam and proton target, holding field direction and detector efficiency changes with time, or small misalignments of the monitors and detectors. To minimize the influence of systematic errors on the difference of the analyzing powers, in addition to the use of the mirror-symmetric detector setup, polarized beam and target runs were interleaved nominally every (12 h) shift. The spin polarization direction of the proton beam was frequently flipped (as described above) at the ion source with random spin-flip selection of the ''up'' or ''down'' states. The spin polarization and the holding field direction of the FST were reversed once every day and once every two days, respectively. To cancel the possible spin correlations between the longitudinal polarization of the beam (due to the neutron production reaction and possible inaccurate rotation of the beam polarization) and sideways polarization of the FST (due to a possible misalignment of the holding field) the field direction of the last spin rotation magnet was reversed periodically to have one more set of combinations. A typical four-day cycle covered all 16 combinations of beam or target polarized, spin directions (up or down), holding field directions (up or down) and last dipole magnet polarities (normal or reversed).

To study the background contribution due to quasielastic scattering from the carbon content of the butanol, C(n,np) data were taken with a dummy target which was made of carbon beads replacing the butanol beads such that its density was approximately the same as the butanol target in the absence of hydrogen. The dummy target was operated under exactly the same conditions as the butanol target, and with the same holding field. Dummy target data were taken using the same set of configurations as the butanol data, holding field direction up or down, last dipole magnet field direction normal or reversed, and polarized beam spin polarization direction up or down. Only polarized beam data were required, since the average of different spin polarization directions would be equivalent to incident unpolarized beam provided the amounts of data with spin direction up and down are the same.

III. DATA ANALYSIS

The procedure followed in the data analysis was as follows. (Further details of the data analysis and of systematic error tests can be found in Ref. [49].)

A. System parameter study

The system parameters recorded during data taking were the proton and neutron beam polarization (polarimeter data), proton beam energy (BEM data), SEM asymmetries, LD_2 target temperature and pressure, holding field strength (Hall probe readings), neutron beam intensity profiles, and proton target (FST) polarizations (at the beginning and the end of the polarized target cycle). Events with charged particles penetrating the neutron button counters (button events) were recorded to calibrate the horizontal positions in the neutron scintillation bars and their pulse heights. The above parameters could affect the systematic errors, and thus they were monitored on-line and kept to specified values within very tight limits. A more detailed analysis of the parameters was carried out off-line.

The average energy of each run, which took on average 1–1.5 h of beam time, was calculated using BEM data. A distribution of the average beam energies yields $\sigma = 0.038$ MeV (for all the data). A few runs with average energies outside a window of ± 0.05 MeV were excluded from the analysis.

After correcting for the instrumental asymmetries, the measured asymmetries of a given polarimeter target of the IBP and CSB polarimeters consisted of contributions from both the hydrogen and nonhydrogenous components of the target material. Effective analyzing powers were calculated from the free pp analyzing power by multiplying with a correction factor α to account for the nonhydrogenous contents of the polarimeter targets. $A_{\rm eff} = \alpha \cdot A_H^{\rm PSA}$ where $A_H^{\rm PSA}$ is the pp elastic scattering analyzing power taken from phase-shift analyses [40]. A typical value of α for the CSB polarimeter with a Kapton target was 0.98–0.99. There are minor differences between the two proton polarization measurements; the ratio varied slightly over the run periods. The IBP polarimeter had larger solid angle coverage which caused higher accidental rates and non-negligible variation of the analyzing power over the polarimeter angular range. The change in the ratio of the polarizations with time shows the

hydrogen loss of the para-xylylene target. Because of its smaller acceptance and lower counting rate, the proton beam polarization measurement with the CSB polarimeter was considered more reliable than the one with the IBP polarimeter. This could be seen in the ratios of the measured neutron polarization to the measured proton polarization.

The SEM left-right (horizontal) and down-up (vertical) asymmetries were calculated from their integrated current signals. The SEM asymmetries were calibrated with respect to beam position offsets by steering the beam away from the established center position by a known amount. The beam position was determined by a beam profile wire monitor. This calibration gave an estimate of the SEM asymmetry with about 0.15 corresponding to a beam centroid offset of ~ 1 mm. A beam position stability of better than ± 0.03 mm was achieved. This implied stability of the proton beam direction to better than $\pm 0.002°$.

The temperature and the pressure of the LD_2 target were monitored at regular intervals and at least once every 8 h during the data taking periods. The density of the LD_2 was calculated from the recorded temperature and pressure data. The density fluctuations of the LD_2 target during the data taking were all within $\delta\rho \leqslant \pm 0.0005$ g/cm^3.

The neutron polarizations were calculated from the measured asymmetries in the two neutron polarimeters after correction for instrumental asymmetries. The effective analyzing power for the OLD neutron polarimeter was determined to be $A_{\rm eff}^{\rm OLD} = 0.18 \pm 0.01$, while the effective analyzing power of the NEW neutron polarimeter was $A_{\rm eff}^{\rm NEW} = 0.20 \pm 0.01$. At the position of the NEW neutron polarimeter, the sizable down-up asymmetry was measured for the polarized beam phase; a small left-right asymmetry was also observed corresponding to the induced neutron polarization for the reaction $D(\vec{p},\vec{n})2p$. Only the relative stability of the ratio, P_n/P_p was used as a cross-check with other measurements.

The neutron beam intensity profile monitor information was processed on-line and recorded. Shifts for the neutron beam x and y profile centroids >1 mm were corrected by retuning the proton beam position. Figures 5(a)–5(c) show the horizontal and vertical neutron beam profiles at the location of the profile monitor and a comparison with a Monte Carlo simulation [36]. It was noticed that the horizontal neutron beam profile was displaced towards the right (negative x direction) by about 8 mm. The Monte Carlo simulations [36] showed that this displacement was equivalent to a misplacement of the LD_2 target cell by about 6 mm upstream along the proton beam axis. The actual physical location of the LD_2 cell was surveyed and confirmed to be displaced upstream along the proton beam axis by 6.2 ± 3.9 mm. At the FST location, the horizontal beam profile had a ''flat'' top region ($>90\%$ of maximum intensity) of approximately 80 mm width which was enough to cover the whole FST, even with the beam displacement, and small enough to cause negligible illumination of surrounding materials. The displacement resulted in a small error in the beam direction (0.6 mr), but it was a constant error throughout the experiment and caused negligible error in the zero-crossing angle difference. The vertical beam profile had a ''flat'' top ($>90\%$ of maximum intensity) of about 55 mm at the FST location which was sufficient to cover the whole target cell containing the beads, again small enough to cause negligible illumination of the surrounding materials.

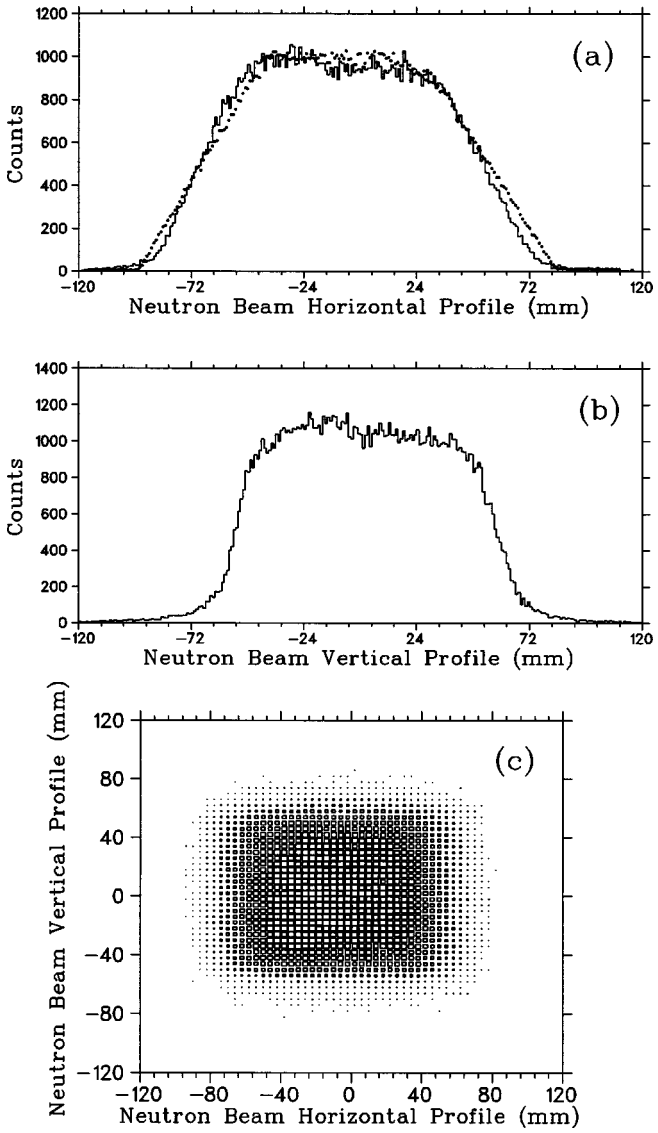

FIG. 5. (a) Horizontal neutron beam profile at the profile monitor location compared to a Monte Carlo simulation, the connected curve represents the data and the discrete curve the simulation; (b) vertical neutron beam profile; (c) neutron beam intensity distribution in the x-y plane.

The zero offsets of the Hall probes, determining the FST holding field strength, were measured before and after every FST polarized measurement. The measured holding field strength showed that a stability and reproducibility of ± 0.3 mT (the average of the two Hall probe readings) was achieved.

The FST polarization was measured at the beginning $[P(t_1)]$ and at the end $[P(t_2)]$ of each polarized target measurement phase with the calibrated NMR system. An exponential function was used to interpolate the average polarization for each data run: $P(t) = P(0)\, e^{-t/\tau}$, where τ is the temperature-dependent decay constant of the polarization. The NMR system was calibrated several times before, between and after each data taking period. Four thermal equilibrium (TE) calibrations were performed during the final data taking period. The largest difference in the NMR cali-

brations was 0.59%. An error of 2% was assigned to the polarizations measured during the final data taking period. This value of 2% was based on a comparison to the earlier calibration of the NMR system in an pp elastic scattering experiment to an accuracy of 2.6% where the error was dominated by the reproducibility of the NMR value ($\pm 2\%$) [46]. Since there was only one TE calibration of the NMR system made during the second data taking period, the overall FST polarization measured in the experiment was estimated to be known to $\pm 3\%$. The average FST polarization for the final data taking run was 85.6%, which was used to determine the slope of the analyzing power $dA_p/d\theta$. The average FST polarization of all the polarized target data was 73.2%.

The position of the FST cell and its filling by the butanol beads were surveyed during and after each data taking period by x-ray radiography. The measured offsets of the FST cell from the target central position (about ± 2 mm) and the filling level of the cell were taken into account in the subsequent data analysis.

Kinematically well-defined (in angle and energy) charged particles, penetrating the ''button'' counters behind the neutron scintillator detectors and therefore called ''button events,'' were used to calibrate the position and the pulse height. A position resolution of $\sigma = 16$ mm was determined from the observed position differences of the button events in the front and rear banks of the scintillator bars. During data taking, high voltages applied to the PMT's were adjusted by matching centroids of the ADC distributions of the button events to nominal values. Small differences in the pulse heights were matched by software rescaling to better than 1 ADC channel.

B. Selection of elastic scattering np events

The recoil proton tracks were reconstructed from their signatures in the DLC's. To determine the ''true'' coordinates in the DLC's, geometrical and measured pulser positions were used as reference points. The typical widths of the pulser peaks were $\sigma = 0.5 - 1.0$ ns which gave an error in the mean of 0.005–0.010 ns for a typical data taking run. The separation of two pulser peaks in terms of the delay line time difference was about 1550 ns. The physical separation of the pulser positions was 552.5 ± 0.7 mm [47]. Typical resolutions of the reconstructed proton coordinates at the DLC locations were ± 1 mm for horizontal coordinates and ± 0.6 mm for vertical coordinates.

The proton vertices were reconstructed by projecting the reconstructed tracks to the y-z plane ($x = 0$) at the center of the FST (z axis is along the neutron beam direction, y axis is along the vertical pointing up, and x axis is towards the left looking downstream, forming a right-handed coordinate system). Because the holding field deflected the proton tracks and shifted the reconstructed proton vertices differently depending on the holding field direction, a shift of a few mm in the z vertices was observed when the holding field changed direction. Therefore, only a loose cut could be applied to the reconstructed vertices.

The DLC efficiencies were about 95% each for the front pair and about 98% each for the rear pair at a proton beam current of about 2.5 μA. Some runs were rejected when the efficiency changed by more than a few percent. Since each group contained two chambers and the minimum number of good coordinates was one x and one y, the combined efficiencies of each group were 99.75% and 99.96% for the front and rear pair of DLC's, respectively.

The recoil proton time-of-flight was measured between the proton TOF ''start'' scintillation counter (pTOF) and two TOF ''stop'' scintillation E counters (E1 and E2) (see Figs. 3 and 4). Timing (TDC) signals were required from both of the pTOF PMT's (top and bottom); the time average of the top and bottom TDC's was used as the proton TOF start signal. Each E counter was subdivided into five sections of a 18×28 grid. Three, or all four, timing signals from a total of 4 PMT's of each E counter were required depending on the section in which a hit occurred. In the center region, valid timing signals from all four PMT's were required to be present, and the time average of all four was used. In the other four regions only three timing signals were required, and the time average of the three PMT's timing signals was used to calculate the stop time. This was because in the regions at any of the four corners, one of the PMT's accepted light mainly from reflections in the scintillator and these reflections would degrade the timing resolution. Since the average absolute time of 3 or 4 TDC's was position dependent (due to the time differences for light traveling within the scintillator to the PMT's), a correction table which was an 18×28 matrix corresponding to the 18×28 grid of each E counter was used to correct for this effect. The size of a cell of the grid was chosen so that the intrinsic time spread for light to cross the cell was much smaller than the resolution of the detection system. The correction constants for adjacent cells within the same section of a grid differed from each other by a few TDC channels (50 ps/per TDC channel).

The proton path lengths from the pTOF counters to the hit points at both E counters were calculated using the reconstructed tracks and the projected coordinates of the tracks at these detector locations. The proton kinetic energy (E_p) was calculated from the known path length and TOF. This calculated energy represented the average energy of the proton from the pTOF counter to the E counters. In order to deduce the proton energy at the scattering point in the FST, a function based on a further Monte Carlo simulation was used. Figure 6 shows the proton kinetic energy distribution, E_p, and the difference, ΔE_p, of the measured and kinematically expected proton energy at the given corrected proton polar angle. An average resolution of 9.0 MeV was obtained in ΔE_p after the E counter calibrations.

To establish the correspondence between the measured proton polar angle and kinetic energy at the scattering point, a Monte Carlo simulation was performed which took into consideration the FST holding field deflection, and multiple scattering and energy loss of the protons. Functions were generated which corrected the measured proton polar angle and the kinetic energy as an average effect (averaging between 1.2 and 1.8°) on an event-by-event basis.

The neutron positions at the scattering points in the target were assumed to be along the central vertical axis ($x = 0$, $z = 0$) with y coordinates determined by the proton vertices. A neutron ''track'' was determined by the two points defined above, and the neutron polar and azimuthal angles (θ_n and ϕ_n) were calculated.

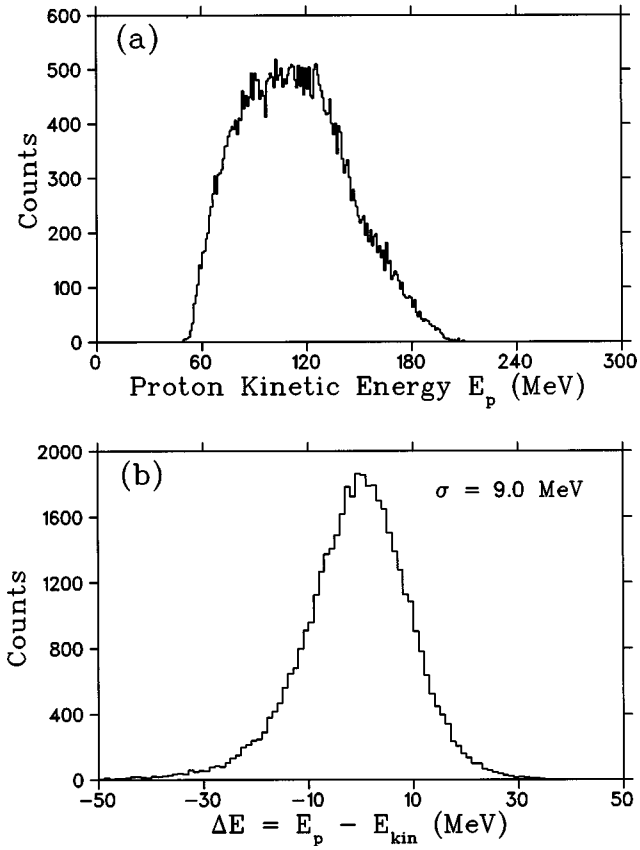

FIG. 6. (a) Distribution of the corrected proton kinetic energy and (b) distribution ($\sigma \simeq 9.0$ MeV) of the difference between the measured proton kinetic energy and the kinematically expected proton energy from the measured proton angle.

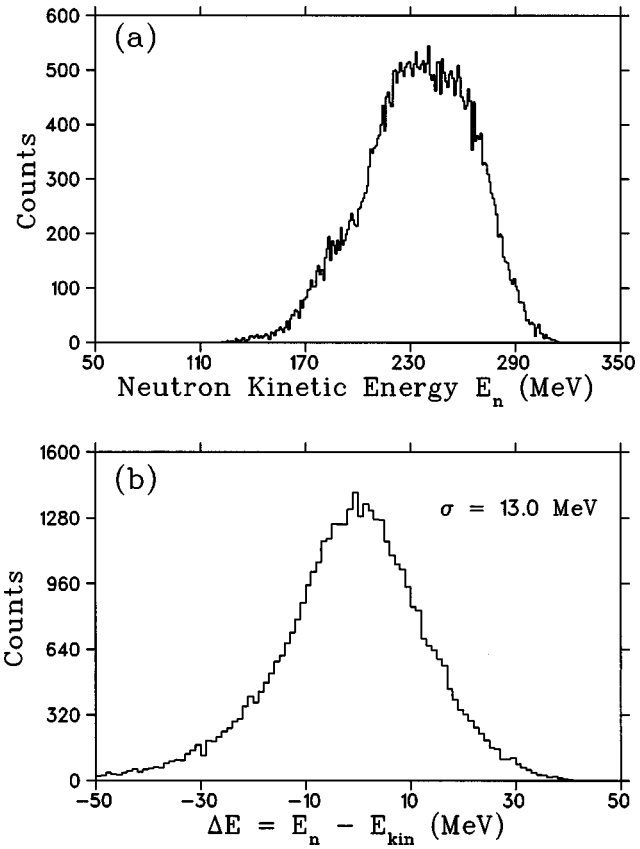

FIG. 7. (a) Measured neutron kinetic energy and (b) distribution ($\sigma \simeq 13.0$ MeV) of the difference of the measured neutron kinetic energy and the kinematically expected neutron kinetic energy at the measured neutron angle.

The neutron kinetic energy was calculated from its TOF and flight distance. The proton arrival time at the pTOF was used as the neutron TOF ''start'' and the neutron arrival time at the neutron array was used as the neutron TOF ''stop.'' The neutron arrival time at the array was taken as the time average of the two ends of the scintillator bar. The neutron TOF was calculated from the time difference between the ''start'' and ''stop'' timing signals, and a timing correction for the coincident proton traveling from the FST to the pTOF was included. The neutron flight distance was calculated from its coordinates at the neutron array and the assumed scattering position. The neutron kinetic energy, E_n, was then obtained from its given flight length and TOF. The difference between the measured kinetic energy and the kinematically expected kinetic energy at the observed neutron angle, ΔE_n, was also calculated (see Fig. 7). An average resolution of $\sigma = 13.0$ MeV was achieved in ΔE_n.

The neutron bar pulse height signals (in ADC channels) after pedestal subtraction were renormalized with reference to the pulse height of the ''simultaneous'' button events (passing protons). The hardware discrimination threshold was in a region where the pulse height distribution was rising rapidly. A typical software threshold of 20 ADC channels (about 1 MeVee) on the neutron bar pulse height was applied to the data. In order to check for possible systematic errors associated with gain changes and the hardware thresholds, software thresholds were varied from 15, 20 to 25 ADC channels.

The neutron beam energy was determined in two ways: one was the sum of the scattered neutron and recoil proton kinetic energies, the other was from the TOF of the neutrons from the LD_2 target to the FST. The energy sum is shown in Fig. 8(c). To calculate the TOF of the neutrons from the LD_2 target to the FST, the rf phase stabilized timing signals were used as the relative timing for the neutron beam TOF ''start'' signal, and of the recoil proton triggered pTOF ''stop'' signal. A timing correction was made for the time-of-flight of the recoil proton from the presumed scattering point to the pTOF scintillator. The incident neutron beam flight distance from the LD_2 target to the FST was 12.85 m. Compared to the summed energies determination, a better energy resolution was achieved due to the use of the phase restricted beam tune in the cyclotron.

For two-body scattering (with known particle masses) at a known energy, one azimuthal angle and any other independent kinematical parameter determine an np elastic scattering event. The over-determined kinematic observables were combined into four variables for χ-square tests for np elastic scattering events:

(1) Opening angle, defined as: $\theta_{\text{open}} = \theta_n + \theta_p - \theta_{\text{kin}}$, where θ_{kin} is the kinematically expected opening angle, $\theta_{\text{kin}} = (\theta_n + \theta_p)_{\text{kin}}$, at the nominal neutron beam energy of 347 MeV. In general, θ_{kin} is a function of θ_n and the incident neutron beam energy (347 MeV in this case) according to energy and momentum conservation and was approximated by a polynomial in θ_n.

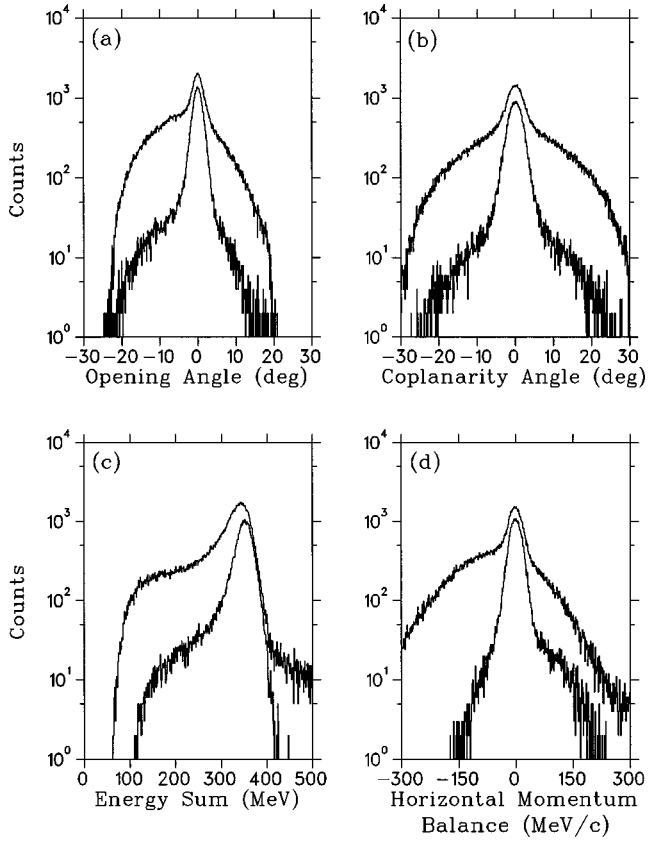

FIG. 8. Distributions of (a) opening angle ($\sigma \simeq 1.3°$), (b) coplanarity angle ($\sigma \simeq 1.9°$), (c) kinetic energy sum ($\sigma \simeq 17.0$ MeV), and (d) horizontal momentum balance ($\sigma \simeq 16.8$ MeV/c) before (upper curves) and after (lower curves) the cuts.

(2) Coplanarity angle, defined as: $\phi_{\text{coplan}} = \phi_n - \phi_p - 180°$. Vertical (perpendicular to the scattering plane) momentum conservation requires $\phi_{\text{coplan}} = 0$.

(3) Kinetic energy sum, defined as: $E_{\text{sum}} = E_n + E_p$. Energy conservation determines E_{sum} to be the same as the incident neutron beam energy.

(4) Horizontal momentum sum, defined as: $\Delta p_x = p_{n,x} + p_{p,x}$, where $p_{n,x}$ and $p_{p,x}$ are the x components of the scattered neutron and recoil proton momenta. Horizontal momentum conservation requires $\Delta p_x = 0$ since the initial particle momentum was along the z axis.

Momentum-dependent χ-squares of these four variables were calculated for every event: $\chi_i^2 = (x_i - x_i^0)^2/\sigma_i(p)^2$, where $\sigma_i(p)$ is the momentum dependent σ of the distribution of each variable determined from the data, x_i is one of the kinematic variables as measured, and x_i^0 is the nominal centroid of the variable. Different χ^2 tests were applied to the data. These tests were either the individual χ square: $\chi_i^2 \leqslant 9$, 7.5, 5, or the sum of the χ squares of the four different variables: $\chi_{\text{sum}}^2 = \Sigma \chi_i^2 \leqslant 20$, 15, 10. Figure 8 shows the distributions for the kinematic variables before and after the cuts on the other variables at $\chi_i^2 \leqslant 7.5$.

For the np coincident events passing the software cuts, scattering asymmetries were calculated. In order to cancel systematic errors to second order, an ''overlap'' method (which takes only the common angular acceptance region of the detector system for different experimental configurations, i.e., holding field direction up or down) was used, and a

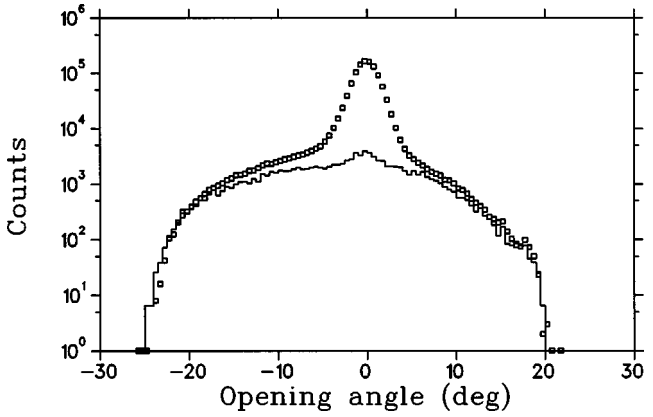

FIG. 9. Opening angle distribution of the carbon data (bottom curve) and the FST data (top curve) for normalizing the tails and estimating the carbon contribution to the FST data.

combination was made of different spin states (up or down) and physical orientations (left or right event). A total of eight asymmetries were calculated for beam or target polarized, holding field up or down, last dipole magnet field direction normal or reversed, using the following equations:

$$\epsilon = \frac{r-1}{r+1}, \tag{8}$$

$$r = \left[\frac{N_L^+ N_R^-}{N_L^- N_R^+}\right]^{1/2}, \tag{9}$$

where the superscripts indicate the initial proton spin polarization directions. The measured asymmetries were fitted to the following function:

$$\epsilon = c_0[(\theta - \theta_\bigcirc) + c_1(\theta - \theta_\bigcirc)^2 + c_2(\theta - \theta_\bigcirc)^3], \tag{10}$$

where $\theta_\bigcirc$ is the zero-crossing angle to be determined from the measured asymmetry, and c_0 is the slope of the asymmetry at the zero-crossing angle and is proportional to the slope of analyzing power multiplied by the value of the corresponding beam or target polarization:

$$c_0 = \left.\frac{d\epsilon}{d\theta}\right|_{\theta_\bigcirc} = P\frac{dA}{d\theta}. \tag{11}$$

The zero-crossing angles for A_n and A_p were obtained as an average of the extracted zero-crossing angles with the above fitting process applied to different holding field (up or down) and last dipole magnet field directions (normal or reversed). The nonzero difference of the zero-crossing angles for A_n and A_p is then due to charge symmetry breaking.

C. Corrections for residual quasielastic background

Background data obtained with the dummy target were analyzed in the same manner as the FST data. Identical sets of cuts were applied. Figure 9 shows the opening angle spectrum for the dummy target data. Clearly, hydrogen peaks are also present. These were due to a hydrogen-containing resistor at the bottom of the FST and superinsulation material around the target. To estimate the ''true'' carbon back-

ground, three different ways of implementing cuts in the off-line analysis of the dummy target data were used:

(1) A cut on the y vertex reduced the hydrogen contribution from the resistor but it leaves the hydrogen contribution from the super-insulation material;

(2) Cuts of $1 \leqslant \chi_i^2 \leqslant 7.5$ removed both the hydrogen peak, and the carbon contribution underneath it as seen in the opening angle distribution. A correction factor was calculated to compensate for the carbon contribution underneath the hydrogen peak. There were uncertainties in estimating both the carbon contribution within the $\chi_i^2 \leqslant 1$ window and the hydrogen contamination to the data inside $1 \leqslant \chi_i^2 \leqslant 7.5$ (i.e., due to multiple scattering);

(3) Through a combination of the FST data and the dummy target data, the carbon contribution was estimated. The FST data after cuts were used to estimate the hydrogen contribution to the dummy target data by subtracting the hydrogen peak in the dummy target data with scaled ''clean'' FST data.

For the results involving individual χ_i^2 cuts, the carbon background contribution to the FST data was obtained by normalizing the tails of the opening angle distributions of the dummy target data to the FST data (Fig. 9). Similar results were obtained for the carbon background contribution to the FST data with the methods (2) and (3) above. A 25% uncertainty in the determination of the background contribution was assumed, which includes uncertainties in normalization, hydrogen contamination elimination from the background data and the different analysis procedures (as described above). The carbon data were further used to evaluate the analyzing powers of the remaining (n,np) background with the given cuts. For this purpose, only method (3) was used, because it gave the largest ''net'' carbon yield, and therefore the least statistical uncertainty of the deduced background analyzing power. The asymmetry distribution of the carbon data was calculated in the same manner as the FST data, and the same fitting function and fitting procedure were used to determine the analyzing power of the background at the A_n zero-crossing angle. For the results involving $\chi_{\rm sum}^2$ cuts, the carbon contributions and the analyzing powers for the various cuts were estimated by comparing the yields and scaling to the results of the individual χ_i^2 cuts. The free np analyzing power, the measured analyzing power with background, and the analyzing power of the background have the following relationship:

$$A_{\rm true} = \frac{A_{\rm measured} - r_b A_{\rm background}}{1 - r_b}, \tag{12}$$

where r_b is the ratio of background contribution to the elastic-scattering contribution. The carbon contribution affects the zero-crossing angle of the analyzing power with the beam polarized (A_n) but not the zero-crossing angle of the analyzing power with the target polarized (A_p). Thus, a correction for the carbon contribution was applied to the zero-crossing angle of the polarized beam data. However, the slopes of the measured asymmetries for both polarized beam and polarized target were affected by the carbon contribution. This was taken into consideration when the slope of A_p was evaluated. Corrections due to background on the zero-crossing angles of A_n were calculated from the background data with different cuts. The corrected zero-crossing angles of A_n were compared to the results from a bin-by-bin subtraction of the carbon data from the FST (butanol) data. The two procedures gave consistent results.

D. Corrections for effective neutron beam energy and polarization

The effective average neutron beam energies of the polarized and unpolarized beams differed by a small amount due to the correlation between the beam energy and the polarization in the $D(\vec{p},\vec{n})2p$ reaction. A correction was required to account for this difference. The experiment was conducted at a neutron beam energy peaked at about 350 MeV with a distribution of FWHM about 11 MeV and an average energy of 347 MeV. The neutron beam energy as well as polarization distributions were simulated with a Monte Carlo simulation [36].

For the polarized and unpolarized beam, the average neutron beam energy was calculated from

$$\overline{E}^{\rm polarized} = \frac{\Sigma P_i^2 \cdot N_i \cdot E_i}{\Sigma P_i^2 \cdot N_i} \quad \text{and} \quad \overline{E}^{\rm unpolarized} = \frac{\Sigma E_i \cdot N_i}{\Sigma N_i}, \tag{13}$$

respectively. The difference of the beam energies was found to be

$$\Delta\overline{E} = \overline{E}^{\rm polarized} - \overline{E}^{\rm unpolarized} = (0.54 \pm 0.11) \ \ \text{MeV},$$

based on the Monte Carlo simulations (the quoted error is an estimate and is discussed below). The variation of the zero-crossing angle with respect to the beam energy was taken from phase-shift analyses [40] to be

$$d\theta_{\bigcirc}/dE_{\rm nbeam} \simeq (-4.75 \pm 0.25) \times 10^{-2} \ \ \text{deg/MeV}.$$

The uncertainty here is an estimate of the systematic error of the phase-shift analyses. The 0.54 ± 0.11 MeV difference of beam energy will give a difference of $+0.026 \pm 0.005$ degree in the zero-crossing angle of A_n.

E. Slope of the analyzing power near zero-crossing angle

To interpret the finite difference of the zero-crossing angles in terms of the difference of the analyzing powers, the slope of the analyzing powers at the zero-crossing angle $(dA/d\theta)$ is required. In principle, this parameter could be obtained from phase-shift analyses [40]. Unfortunately the phase-shift analysis results over the last few years show about 10% discrepancies. For the polarized target measurement (A_p) where the FST polarization was known to better than $\pm 2\%$ as discussed above, the slope of the analyzing power around the zero-crossing angle was determined from

$$\frac{dA_p}{d\theta} = \frac{1}{1 - r_b} \ \frac{1}{P_{\rm FST}} \ \frac{d\epsilon_p}{d\theta}, \tag{14}$$

where r_b is the ratio of the background contribution to the np elastic events, $P_{\rm FST}$ is the average polarization of the FST

and $d\epsilon_p/d\theta$ is the measured slope of the asymmetry. The quasielastic background did not affect the zero-crossing angle determination of the polarized target data, but it diluted the slope of the measured asymmetry giving the correction term $1/(1-r_b)$. The resulting slope of the analyzing power was determined to be

$$\frac{dA_p}{d\theta} = (1.35 \pm 0.05) \times 10^{-2} \text{ deg}^{-1},$$

where the error is due to the uncertainty in the absolute value of the FST polarization, systematic errors as deduced by different χ^2 cuts, and the uncertainty in the correction for the background dilution.

F. The shape of $\Delta A(\theta)$

The angular distribution of the difference of the analyzing powers is important because of its sensitivity to the different CSB contributions, in particular the $\rho^\circ - \omega$ mixing contribution. However, there is an intrinsic difficulty to extract the angular distribution as pointed out above

$$\epsilon_n - \epsilon_p = \langle A(\theta) \rangle \cdot \Delta P + \Delta A(\theta) \cdot \langle P \rangle. \tag{15}$$

In this experiment, the average neutron beam polarization $\overline{P_n} = 61.2\% \pm 1.8\%$ and the average FST polarization $\overline{P_p} = 73.2\% \pm 2.2\%$ or $\langle P \rangle \equiv (\overline{P_n} + \overline{P_p})/2 = 67.2\% \pm 1.4\%$ and $\Delta P \equiv \overline{P_n} - \overline{P_p} = -12.0\% \pm 2.8\%$. Here, the error in the neutron beam polarization was estimated to be $\pm 3\%$ which is the quadrature sum of the estimated $\pm 2\%$ uncertainty in the proton beam polarization (the effective pp analyzing power of the CSB polarimeter) and the $\pm 2\%$ uncertainty in the average of $\sqrt{r_t^2 + r_{t'}^2}$. To obtain $\Delta A(\theta)$ at the 10^{-4} level, the polarizations would need to be known to a level not attainable at present. The best one can determine is

$$\text{``}\Delta A(\theta)_{\text{expt}}\text{''} = \Delta A(\theta)_{\text{true}} + c \cdot A(\theta). \tag{16}$$

Here c is directly related to the uncertainty of $\Delta P/\langle P \rangle$. The IUCF experiment [7] extracted the component of $\Delta A(\theta)$ which is ''uncorrelated'' with $A(\theta)$ by adjusting c until the variance $(\langle \text{``}\Delta A\text{''}^2 \rangle - \langle \text{``}\Delta A\text{''} \rangle^2)$ of the ''$\Delta A(\theta)$'' data set reached a minimum. In this manner, a 12-point angular distribution of ''ΔA'' was obtained within limitations imposed by uncertainties in the measured beam and target polarizations. At the TRIUMF experimental energies (477 and 347 MeV), the angular distribution of $\Delta A(\theta)$ near the zero-crossing angle of the analyzing powers has a shape similar to the analyzing power, $A(\theta)$, itself. Therefore, the minimum variance method used in the IUCF experiment can not be applied. In principle, if the theoretical prediction of the zero-crossing angle of ΔA was very accurate and if the asymmetries at that angle could be measured very accurately, then $\Delta P/\langle P \rangle$ could be determined in the experiment and the angular distribution of ΔA could be extracted. In lieu of the latter, a comparison of the shape of ΔA with theoretical predictions can be made as the only alternative by adjusting the constant c until the chi-square between the measurement and the calculation is minimized

$$\text{``}\Delta A(\theta)_{\text{expt}}\text{''} = \Delta A(\theta)_{\text{theory}} + c \cdot A(\theta), \tag{17}$$

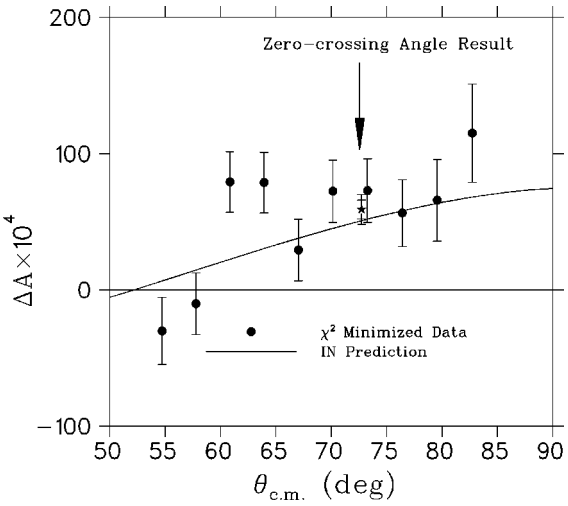

FIG. 10. The shape of $\Delta A(\theta)$. The solid curve is from Iqbal and Niskanen's predictions [15]. The solid circles are obtained from the χ^2 minimization between the experimental data and theoretical predictions by varying c of Eq. (17). The error bars on the experimental data shown in the figure are statistical errors only. The ''star'' point is the experimental result at the zero-crossing angle; the inner error bar is the statistical error and the outer error bar is the quadrature sum of the systematic and statistical errors.

''$\Delta A(\theta)_{\text{expt}}$'' was obtained from the measured asymmetries and $\Delta A(\theta)_{\text{theory}}$ was taken to be the predicted theoretical distribution of Iqbal and Niskanen [15]. A ten-point distribution giving the shape of ΔA was obtained (Fig. 10).

IV. SYSTEMATIC ERRORS

Various estimates of the systematic errors were made with assumed system parameters. Details of the systematic error estimates can be found in Ref. [49]. Based on these estimates, very stringent limits were applied to the system parameters during the experiment in order to constrain the individual systematic error contributions to ΔA to below 10^{-4} at the zero-crossing angle (these limits also apply constraints to the systematic errors away from the zero-crossing angles). Table II shows that indeed all systematic errors at the zero-crossing angle are below the 10^{-4} level except for the uncertainty due to background contribution which will be further discussed. Background contributions also dominate the systematic errors away from the zero-crossing angle as shown in Table II.

Estimates of the systematic errors were also made by applying different tests on the data and investigating the variations of ΔA with the cuts. Different χ^2 cuts were applied to the data to eliminate the background due to C(n,np) and to study the resulting errors of the residual background and possible bias to the cuts on the smeared distributions. The cuts included individual χ^2 cuts of $\chi_i^2 \leqslant 5$, 7.5, 9 and summed χ^2 cuts of $\chi_{\text{sum}}^2 = \Sigma \chi_i^2 \leqslant 10$, 15, 20, where i represents opening angle, coplanarity, energy sum and horizontal momentum balance as defined above. Different χ^2 cuts represent sampling different portions of the data within the same data set and provides different statistical significance. Individual or

TABLE II. Summary of the estimates of the systematic errors in the difference of the analyzing powers.

Sources of systematic error	Experimental parameters	Contribution to $\delta(\Delta A)$ at $A=0$	Contribution to $\delta(\Delta A)$ at $A=0.2$[a]
Proton beam energy shift	0.038 MeV	3×10^{-5}	3×10^{-5}
Proton beam spot modulation at the LD_2 target	0.03 mm	1×10^{-5}	1×10^{-5}
Proton beam angle modulation	0.005°	1×10^{-5}	1×10^{-5}
LD_2 density stability	0.0005 g/cm^{-3}	$<10^{-5}$	$<10^{-5}$
Irreproducibility of holding field (HF)	<0.3 mT	$<7\times10^{-5}$	$<7\times10^{-5}$
Δr of FST wrt HF	0.5 mm	3×10^{-5}	3×10^{-5}
Inequality of up/down polarization	0.05	0	2×10^{-5}
$P_{p\text{beam}}$ precession	$\sim3^0$	$\ll10^{-4}$	$\leqslant2\times10^{-5}$
$P_{n\text{beam}}$ precession	$\sim3^0$	$\ll10^{-4}$	$\leqslant2\times10^{-5}$
HF tilt	$<0.5^0$	$<5\times10^{-5}$	5×10^{-5}
Residual P_n on polarized FST	$\chi\sim3^0$,	$\ll10^{-4}$	1×10^{-5}
	$\phi=0.5^0$	$\ll10^{-4}$	$\leqslant1\times10^{-4}$
Misalignment of detectors	0.03^0	$\ll10^{-4}$	$\ll10^{-4}$
Multiple scattering in FST	$<0.7^0$	$\ll10^{-5}$	$\ll10^{-5}$
Neutron detector instability	$\leqslant0.3\%$	$\leqslant2\times10^{-5}$	$\leqslant2\times10^{-5}$
Residual background asymmetry	$\leqslant\pm1\%$	2.8×10^{-4}	7×10^{-4}
		$A_b=(-4\pm7)\times10^{-3}$	$A_B=(6\pm2)\times10^{-2}$

[a]Not including those errors due to uncertainties of ΔP as discussed in Sec. III. The value of $A=+0.2$ is reached at $\theta_{\text{c.m.}}=60°$ towards the lower limit of the angular acceptance. The sign $\ll$ implies at least a factor 10 smaller.

summed χ^2 cuts provides the same statistical significance but provide different sampling of the data and therefore aids in understanding possible bias of the cuts. After hardware and then software gain matching of the neutron bar ADC signals, different software thresholds were applied to the data to study the systematic errors associated with the neutron bar efficiency. A systematic error limit based on the different software thresholds, and therefore possible neutron detector efficiency variations, was deduced. Systematic errors were also studied by fitting the asymmetries with different angular ranges and extracting the zero-crossing angles. At the extremes of the detection system, the data have larger statistical uncertainties and may also have larger systematic errors. In general systematic errors increase with increasing $A(\theta)$. After all cuts had been applied and the background contribution of quasielastic scattering from nonhydrogenous contents of the target material had been subtracted, the systematic errors due to a residual background were estimated. There were two possible sources of errors associated with the background; one was the uncertainty in determining the ratio of the background contribution to the elastic-scattering events after the cuts, and the other one was the uncertainty of the background analyzing power. The uncertainty in the ratio of the background contribution to the elastic scattering events was estimated to be 25% (i.e., a 1% uncertainty with a 4% background). Combining the two factors, the systematic errors associated with the background subtraction and correction were deduced. The effective average beam energy difference for the polarized and unpolarized neutron beam was corrected with the result from Monte Carlo simulations [36]. The systematic errors associated with this were estimated by assuming that the correction was accurate to about 20% (upper limit) of the total difference $\Delta E=0.54$ MeV, or $\delta(\Delta E)=0.11$ MeV. Systematic errors on the zero-crossing angle difference and the difference of the analyzing powers were so deduced. A summary of all systematic errors described above is shown in Table III for the difference in the zero-crossing angles and in Table IV for ΔA away from the zero-crossing angles (e.g., $A=0.2$). The quadrature sum of the different systematic errors was used in the final result. For systematic errors in ΔA away from the zero-crossing angles, there is an additional contribution due to uncertainties in ΔP. This uncertainty is used as an adjustable parameter when the shape of ΔA is compared with theoretical predictions.

V. RESULTS AND DISCUSSION

The difference of the center-of-mass zero-crossing angle of the analyzing powers for np elastic scattering at 347 MeV is determined to be

TABLE III. Summary of the systematic errors in the difference of the zero-crossing angles.

Item	$\delta(\Delta\theta_{\bigcirc})$
Different cuts	0.031°
Background	0.021°
Nbar ADC cuts	0.028°
Different fits	0.019°
$E_{n\text{beam}}$ correction	0.005°

TABLE IV. Summary of the systematic errors in the difference of the analyzing powers at the borders of the angular range covered (e.g., at $A=0.2$).

Item	$\delta(\Delta A)$
Different cuts	18×10^{-4} [a]
Background	7×10^{-4}
Nbar ADC cuts	3×10^{-4}
Different fits	9×10^{-4} [a]
$E_{n\text{beam}}$ correction	1×10^{-4}
Total	21×10^{-4}

[a]These two items are strongly affected by the edge effects of acceptance. If $A=0.1$ is considered, these terms reduce by more than a factor of 2.

$$\Delta\theta_{\bigcirc} \equiv \theta_{\text{c.m.}}(A_n=0) - \theta_{\text{c.m.}}(A_p=0)$$
$$= 0.438^\circ \pm 0.054^\circ \text{ (stat.)} \pm 0.051^\circ \text{ (syst.)},$$

based on fits of the measured asymmetry angular distributions over the angle range $53.4^\circ \leqslant \theta_{\text{c.m.}} \leqslant 86.9^\circ$ in the center-of-mass system. The first error gives the statistical error and the second error is the systematic error which is obtained as the quadrature sum of the various contributions. The slope of the analyzing power A_p at its center-of-mass zero-crossing angles is given by

$$\frac{dA_p}{d\theta_{\text{c.m.}}} = (-1.35\pm0.05)\times10^{-2} \text{ deg}^{-1},$$

based on least-squares fits of the asymmetry curves and the average proton target (FST) polarization. The error here is dominated by the uncertainty in the FST polarization and the estimated systematic errors from different cuts and the background subtraction. Using the slope of the analyzing power A_p and assuming $d\langle A(\theta_{\bigcirc})\rangle/d\theta_{\text{c.m.}} = dA_p/d\theta_{\text{c.m.}}$, the difference of the analyzing powers at the zero-crossing angle, where $\langle A(\theta)\rangle = 0$, is

TABLE V. Numerical results of the measured, χ^2 minimized and predicted [15] $\Delta A(\theta)$.

$\theta_{\text{c.m.}}$	$\Delta A(\theta)$ measured	$\Delta A(\theta)$ χ^2 minimized	$\Delta A(\theta)$ predicted
(deg)	10^{-4}	10^{-4}	10^{-4}
82.72	(78.5 ± 36.1)	(115 ± 36.1)	68.0
79.55	(39.4 ± 30.0)	(65.7 ± 30.0)	63.4
76.40	(41.2 ± 24.5)	(56.3 ± 24.5)	58.0
73.26	(70.4 ± 23.3)	(72.8 ± 23.3)	51.8
70.13	(82.8 ± 22.8)	(72.3 ± 22.8)	45.0
67.02	(53.7 ± 22.6)	(29.2 ± 22.6)	37.8
63.92	(116 ± 22.3)	(78.7 ± 22.3)	30.2
60.84	(131 ± 22.2)	(79.1 ± 22.2)	22.3
57.77	(53.7 ± 22.5)	(-10.2 ± 22.5)	14.4
54.71	(44.5 ± 24.6)	(-30.2 ± 24.6)	6.45

$$\Delta A = -\frac{d\langle A(\theta_{\bigcirc})\rangle}{d\theta_{\text{c.m.}}}\cdot\Delta\theta_{\bigcirc}$$
$$= [59\pm7\text{ (stat.)}\pm7\text{ (syst.)}\pm2\text{ (syst.)}]\times10^{-4}.$$

Here the first error is the statistical error, the second error is the systematic error, and the third error is an additional systematic error due to the uncertainty in the slope parameter $dA_p/d\theta_{\text{c.m.}}$. The shape of $\Delta A(\theta)$ is shown in Table V and Fig. 10. A $\chi^2=18.7$ for a total of 10 points is obtained from fitting the experimental $\Delta A(\theta)$ to the theoretical predictions of Iqbal and Niskanen [15] by adjusting the value of $c = \delta(\Delta P/\langle P\rangle)$ [see Eqs. (16) and (17)]. One obtains $c = -0.030\pm0.015$. This c is well within the range of uncertainty of $\delta(\Delta P/\langle P\rangle)$ (about $\pm4.2\%$) which follows from the average polarizations of the beam and the FST as discussed above. The individual zero-crossing angles of the analyzing powers and the analyzing power angular distributions at 347 MeV have also been measured. These experimental results will be reported separately.

The nonzero difference of the analyzing powers measured in the present experiment shows clear evidence for charge symmetry breaking and represents the largest effect (6 standard deviations) among the available experimental results on charge symmetry breaking in np elastic scattering. The re-

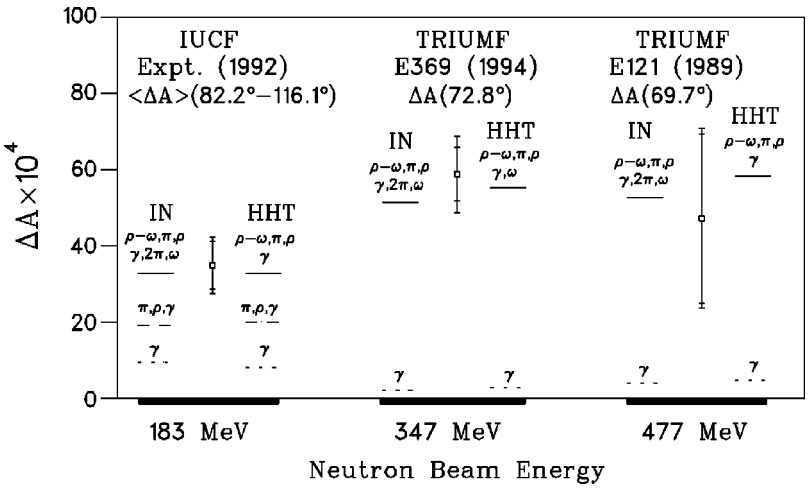

FIG. 11. Summary of the experimental results on CSB in np elastic scattering compared to the theoretical predictions of Iqbal and Niskanen [15] (IN) and Holzenkamp, Holinde, and Thomas [13] (HHT). The inner (smaller) error bars on the data points represent the statistical errors alone and the outer (larger) error bars represent the quadrature sum of the systematic and statistical errors. The horizontal lines are the various summed contributions obtained by IN and HHT.

sults of the experiment, the difference of the analyzing powers $[\Delta A(\theta_{\bigcirc})]$ and the shape of the $\Delta A(\theta)$ in the angular range $53.4° \leqslant \theta_{\text{c.m.}} \leqslant 84.2°$, agree well with the theoretical predictions of Iqbal and Niskanen [15] and Holzenkamp, Holinde, and Thomas [13] [for the latter predictions only $\Delta A(\theta_{\bigcirc})$ is compared] which are based on meson exchange nucleon-nucleon potential models. At 347 MeV, the photon exchange contribution and the dominant one-pion exchange contribution together account for most of the analyzing power difference at the zero-crossing angle. Figure 11 presents a summary of the experimental results on CSB in np elastic scattering compared to theoretical predictions of Iqbal and Niskanen (IN) [15] and Holzenkamp, Holinde, and Thomas (HHT) [13]. The $\rho^0-\omega$ mixing contribution crosses zero at the vicinity of the zero-crossing angles of the analyzing powers, A_n and A_p, and therefore its contribution is small. However, the angular distribution of $\Delta A(\theta)$ depends sensitively on the $\rho^0-\omega$ mixing contribution. In the present experiment, the determination of the shape of $\Delta A(\theta)$ is limited by the larger systematic errors away from the zero-crossing angles.

For incident energies above 300 MeV, the zero-crossing angle of the $\rho^0-\omega$ mixing contribution occurs very closely to the zero-crossing angle of the average analyzing power $\langle A \rangle$, and consequently its contribution to ΔA at the zero-crossing angle of $\langle A \rangle$ is very small. Since the one photon exchange contribution and the one pion (and ρ-meson) exchange contribution can be calculated with confidence, the difference between the measured and calculated ΔA provide an upper limit on the contribution of a parity conserving, time-reversal-invariance nonconserving (and simultaneously charge symmetry breaking) NN interaction. As discussed by Simonius [50] the upper limit on such an interaction so determined compares favorably with almost all experimentally determined upper limits on such an NN interaction. In step with improved calculations one may consider a higher precision measurement of ΔA to lower the present upper limit to the level of what can be deduced from the electric dipole moment of the neutron.

In order to untangle the different contributions to ΔA, it is necessary to perform even higher precision experiments, at energies lower than 300 MeV. An optimum lower experimental energy should be sought to enhance the $\rho^0-\omega$ contribution both to ΔA at the zero-crossing angle as well as to the angular distribution of $\Delta \mathrm{A}(\theta)$. Other classes of CSB experiments can also provide information on the $\rho^0-\omega$ mixing contribution. Another TRIUMF CSB experiment in progress measures the forward-backward asymmetry in the reaction $np \rightarrow d\pi^0$ as a sensitive test of the $\pi-\eta$ mixing contribution [51]. Further detailed studies of CSB in different systems could provide more information on the underlying quark structure of the nucleon, and therefore help to form a direct bridge between phenomenological NN potential models represented by the meson exchange theory and the fundamental theory of QCD describing the strong interaction.

ACKNOWLEDGMENT

Work supported in part by the Natural Sciences and Engineering Research Council of Canada.

[1] E. M. Henley, in *Isospin in Nuclear Physics*, edited by D. H. Wilkinson (North-Holland, Amsterdam, 1969), p. 15.
[2] E. M. Henley and G.A. Miller, in *Mesons in Nuclei*, edited by M. Rho and D. H. Wilkinson (North-Holland, Amsterdam, 1979), p. 407.
[3] G. A. Miller, B. M. K. Nefkens, and I. Slaus, Phys. Rep. **194**, 1 (1990).
[4] G. A. Miller and W. T. H. van Oers, in *Symmetries and Fundamental Interactions in Nuclei*, edited by W. C. Haxton and E. M. Henley (World Scientific, Singapore, 1995), p. 127.
[5] R. Abegg *et al.*, Phys. Rev. Lett. **75**, 1711 (1995).
[6] R. Abegg *et al.*, Phys. Rev. D **39**, 2464 (1989); R. Abegg *et al.*, Phys. Rev. Lett. **56**, 2571 (1986).
[7] S. E. Vigdor *et al.*, Phys. Rev. C **46**, 410 (1992); L. D. Knutson *et al.*, Phys. Rev. Lett. **66**, 1410 (1991).
[8] S. E. Vigdor (private communication) (the value of ΔA changed by about 4% due to a new calibration of the neutron beam polarization and consequent renormalization of the result).
[9] G. A. Miller, Nucl. Phys. **A518**, 345 (1990).
[10] C. Y. Cheung, E. M. Henley, and G. A. Miller, Nucl. Phys. **A348**, 365 (1980).
[11] G. A. Miller, A. W. Thomas, and A. G. Williams, Phys. Rev. Lett. **56**, 2567 (1987).
[12] A. G. Williams, A. W. Thomas, and G. A. Miller, Phys. Rev. C **36**, 1956 (1987).
[13] B. H. Holzenkamp, K. Holinde, and A. W. Thomas, Phys. Lett. B **195**, 121 (1987).
[14] L. Ge and J. P. Svenne, Phys. Rev. C **33**, 417 (1986); **34**, 756 (E) (1987).
[15] M. J. Iqbal and J. A. Niskanen, Phys. Rev. C **38**, 2259 (1988); (private communication).
[16] J. L. Friar and S. A. Coon, Phys. Rev. C **53**, 588 (1996).
[17] J. A. Niskanen and S. E. Vigdor, Phys. Rev. C **45**, 3021 (1992).
[18] T. Goldman, J. A. Henderson, and A. W. Thomas, Few-Body Syst. **12**, 123 (1992).
[19] L. M. Barkov *et al.*, Nucl. Phys. **B256**, 365 (1985).
[20] T. Hatsuda *et al.*, Phys. Rev. C **49**, 452 (1994).
[21] G. Krein, A. W. Thomas, and A. G. Williams, Phys. Lett. B **317**, 293 (1993).
[22] J. Piekarewicz and A. G. Williams, Phys. Rev. C **47**, R2462 (1993).
[23] M. J. Iqbal and J. A. Niskanen, Phys. Lett. B **322**, 7 (1994).
[24] K. Saito and A. W. Thomas, Phys. Lett. B **335**, 17 (1994).
[25] K. L. Mitchell *et al.*, Phys. Lett. B **355**, 282 (1994).
[26] H. B. O'Connell *et al.*, Phys. Lett. B **336**, 1 (1994).
[27] T. D. Cohen and G. A. Miller, Phys. Rev. C **52**, 3428 (1995).
[28] S. A. Coon and M. D. Scadron, Phys. Rev. C **51**, 2923 (1995).
[29] S. Gardner and C. J. Horowitz, Phys. Rev. Lett. **75**, 2462 (1995).
[30] M. J. Iqbal, X. Jin, and D. B. Weinleber, Phys. Lett. B **367**, 45 (1996).

[31] R. Abegg *et al.*, Nucl. Instrum. Methods Phys. Res. A **234**, 11 (1985); **234**, 20 (1985).
[32] A. N. Zelenski *et al.*, Nucl. Instrum. Methods Phys. Res. A **334**, 285 (1993).
[33] L. Brown and C. Petitjean, Nucl. Instrum. Methods Phys. Res. A **117**, 343 (1968).
[34] W. D. Ramsay *et al.*, Nucl. Instrum. Methods Phys. Res. A **327**, 265 (1993).
[35] D. V. Bugg and C. Wilkin, Nucl. Phys. **A467**, 575 (1987); D. V. Bugg (private communication).
[36] L. Gan *et al.*, Nucl. Instrum. Methods Phys. Res. A **365**, 185 (1995).
[37] R. Abegg and R. Schubank, TRIUMF Internal Report, TRI-DN-87-17, 1987 (unpublished).
[38] L. G. Greeniaus and J. Soukup, TRIUMF Internal Report, TRI-DN-81-1, 1981 (unpublished).
[39] Para-xylylene-N obtained from Parmat Inc., 958 Bassett Rd., Cleveland, Ohio 44145.
[40] R. A. Arndt, Interactive dial-in program SAID, 1993; R. A. Arndt, I. I. Strakovsky, and R. L. Workman, Phys. Rev. C **50**, 2731 (1994).
[41] D. A. Hutcheon *et al.*, Nucl. Phys. **A535**, 618 (1991).
[42] C. A. Davis *et al.*, Phys. Rev. C **53**, 2052 (1996).
[43] R. Abegg, TRIUMF Internal Report, TRI-DN-87-25, 1987 (unpublished).
[44] R. Abegg *et al.*, Nucl. Instrum. Methods Phys. Res. B **79**, 318 (1993).
[45] P. P. J. Delheij, D. C. Healey, and G. D. Wait, Nucl. Instrum. Methods Phys. Res. A **264**, 186 (1988).
[46] R. Abegg *et al.*, Nucl. Instrum. Methods Phys. Res. A **306**, 432 (1991).
[47] P. R. Poffenberger, TRIUMF Internal Report, TRI-DN-84-30, 1984 (unpublished).
[48] R. A. Cecil, B. D. Anderson, and R. Madey, Nucl. Instrum. Methods **161**, 439 (1979).
[49] Jianguo Zhao, Ph.D. thesis, University of Manitoba, 1995.
[50] M. Simonius, Phys. Rev. Lett. **78**, 4161 (1997).
[51] A. K. Opper and E. Korkmaz, TRIUMF Experiment 704 proposal (1993).